Soft Matter

ARTICLE TYPE

Cite this: DOI: 00.0000/xxxxxxxxxx

Influence of period and surface anchoring strength in liquid crystal optical axis gratings†

Xiangyu Xue,[a] Inge Nys,[a] Kristiaan Neyts,[a] and Jeroen Beeckman*[a]

Received Date
Accepted Date

DOI: 00.0000/xxxxxxxxxx

Liquid crystal (LC) based geometric phase optical elements are widely used to effectively change the wavefront or propagation direction of light. Using photoalignment, the liquid crystal can be aligned according to the designed pattern, leading to components such as gratings, lenses or general wavefront shaping devices. The functionality and efficiency of the component is strongly influenced by how well the LC follows the imposed alignment pattern. Next to a considerable tilting of the LC at the air interface, we report on the observation of symmetry breaking in polymerized LC polarization gratings. By carefully analyzing the experimental and numerical data for gratings with different periods, we conclude that the non-negligible homeotropic anchoring strength at the air interface is responsible for the tilt angle and the symmetry breaking. The role of anchoring strength at the photoaligned and air interface and other parameters are investigated.

1 Introduction

Traditional optical elements rely on differences in refractive index and geometry to change the phase of the light passing through, such as the well known lenses and prisms. Optical axis gratings formed by liquid crystals (LCs) utilize the principle of the Pancharatnam-Berry (PB) phase or geometric phase[1]. They consist of LCs arranged in periodic rotation with a period of Λ for every 180° rotation of the LC. They have much higher efficiency than conventional gratings and have been used in beam shaping[2], beam steering[3], beam combining[4], wave guiding[5], augmented reality (AR) and virtual reality (VR)[3,6,7]. The photoalignment technology is also widely used nowadays to define the LC anchoring at the substrates and it provides a wide range of possibilities for designing LC optical elements. Compared to the traditional rubbing process, this process does not require physical contact with the substrate surface, thus reducing harmful dust and charges. Photoalignment material forms an alignment pattern by responding to polarized light and well-designed patterns can be written by locally changing the direction of linear polarization of the light beam. One way to spatially define the polarization direction is by using a spatial light modulator (SLM) which modifies the polarization direction of an expanded laser beam pixel by pixel[8]. Another method is to use the interference pattern of two laser beams to make optical axis gratings or optical axis lenses[4,9]. The photoalignment technology can be applied to either LC cells[4,10] with non-polymerizable LC or to single substrate devices on which polymerizable LC is spincoated[11,12]. Devices based on polymerized LC layers are very stable compared to fill-in cells. Moreover the polymerized LC layer can be pulled off from the substrates for different application such as thin film color filters[13] or to create soft robots using 4D print technology[14]. LC polymer elements are fairly easy to fabricate, they have a high optical efficiency and they are very thin as the optical functionality is encoded in a layer of only a few micrometer. In order for LC polymers to achieve their optimal performance and maximum optical efficiency, the alignment quality of LCs prior to photopolymerization is particularly important. Due to different effects, such as surface anchoring energy or elastic distortion energy, the LCs in the bulk may be aligned different from what is imposed by the photoalignment at the surface. It has been demonstrated that slight changes in the fabrication process may lead to out-of-plane tilting of the director near the air interface which in turn leads to the formation of unwanted domains[12]. With respect to complex alignment patterns, a lot of research has been devoted on analyzing the behavior of LCs with crossed assembly of both substrates with 1D periodically rotating alignment[15–20]. It was found that the size of the unit cell doubled compared to what is expected from the initial period of the alignment pattern. Different domains are observed with the director configuration shifted over half a period, sometimes with an opposite tilt of the director. By applying a voltage over the LC layer, the period may be reverted back to the initial period from the alignment pattern. The phenomenon where the actual period is larger than the period imposed by the alignment pattern can be denoted as symmetry breaking.

In theory, the photoalignment pattern can have very short pe-

[a]Liquid Crystals & Photonics Group, Electronics and Information Systems Department, Ghent University, 9052 Ghent, Belgium. E-mail: Jeroen.Beeckman@Ugent.be

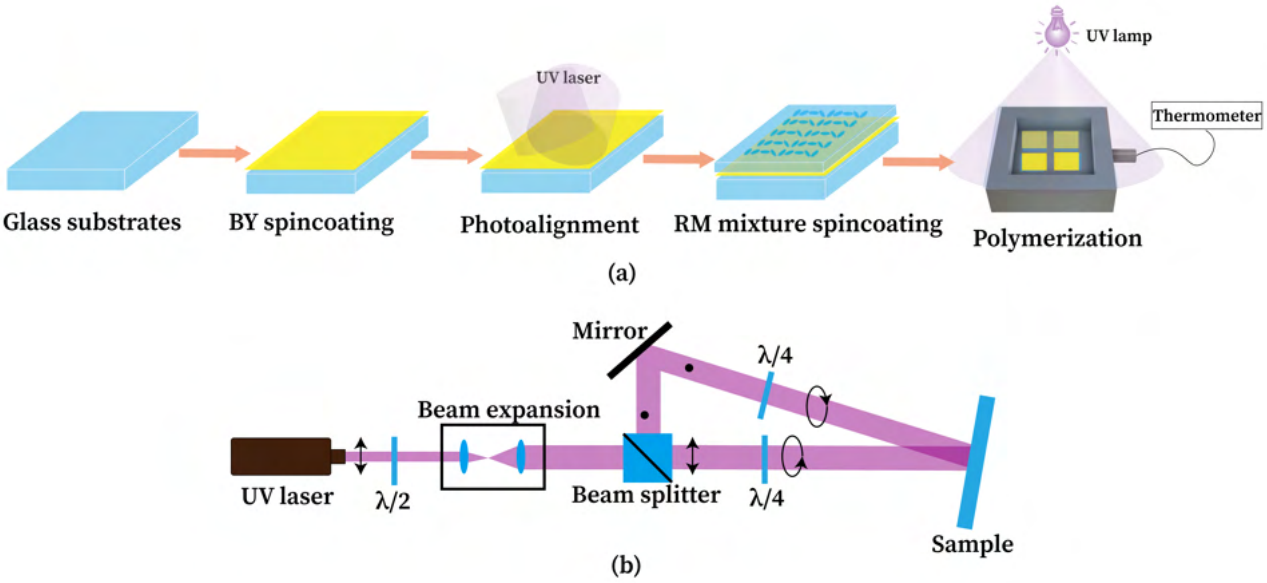

Fig. 1 The fabrication process of polymerized LC optical axis gratings: (a) Flow diagram of key steps in making samples. (b) Optical setup of photoalignment step.

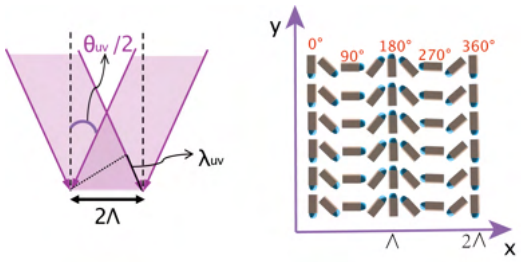

Fig. 2 A sketch of the angular relationship between the LC orientation and the two UV laser beams. Left: sketch of two circularly polarized light beam; Right: example of LC orientation in optical axis gratings.

riod, by simply adjusting the period of the laser interference pattern. When putting liquid crystal on top of such a pattern however, there is limit on the smallest period because of the very high splay-elastic energy that is related to short periods. In practice, it is difficult to realize grating periods smaller than the thickness of the layer. Gratings of 10 μm[21], 5 μm[22] and 3.4 μm[4] have been reported. Kun *et al.* reported optical axis gratings with a period down to 2.2 μm[23]. A grating period of 335 nm has been reported[24], which was made possible by spincoating multiple very thin layers on top of each other (18 layers for a total thickness of 1000 nm). Another way to overcome the limit imposed by the splay-bend elastic energy, is by adding chiral dopants to the LC resulting in short pitch chiral LC gratings that work in reflection mode[25–27]. Unlike filling cells with LC, spin-coating LC on a substrate means that the top surface of the sample is exposed to ambient air, leading to either planer degenerate or hometropic weak anchoring. To understand the behavior of the LC for short periods, optical axis gratings with different periods are fabricated in this work. A vacuum environment instead of a conventional glove box with nitrogen atmosphere[11] is used during the photopolymerization process. The polymerization process happens successfully, but samples with smaller periods differ distinctively from samples with larger period, showing periodic brightness changes with a period of 2Λ length instead of the expected Λ. A threshold period is observed for this symmetry breaking effect. We will demonstrate that this is related to a significant tilt angle of the LC director. This can be explained and modeled accurately by assuming that there is a weak homeotropic anchoring strength at the LC-air interface. Simulations of the director configuration and the associated transmission under crossed polarizers, reveal excellent agreement with experimental observations. Our study provides a better understanding of the behavior of LC optical axis gratings with small periods and can provide insight into which material parameters are desired to reduce the period even further.

2 Sample preparation

2.1 Photoalignment layer

The process of making an optical axis grating is shown in Figure 1 (a). The ITO-coated glass substrate is placed in an ultrasonic cleaner and soaked in soap, acetone, isopropanol, and deionized water for 15 minutes successively. The sheet resistance of ITO is about 100 Ω/sq. After that, the substrate is dried at 100°C for 4 hours and treated in an ozone plasma. Brilliant yellow (BY) is used as photoalignment material to align the LC. BY (Sigma-Aldrich) is dissolved in N, N-dimethylformamide (DMF, from Merck) with a concentration of 0.2 wt%. The solution is then spin-coated onto the glass substrate (3000 rpm, 30 s) and baked for 10 min at 80°C. Next, the BY coated substrate is illuminated by the interference pattern of two laser beams. The laser source is a single-mode continuous wave UV laser (Coherent, Genesis CX SLM, 100 mW) emitting at 355 nm wavelength. As shown in Figure 1(b), the UV laser beam is passing through a

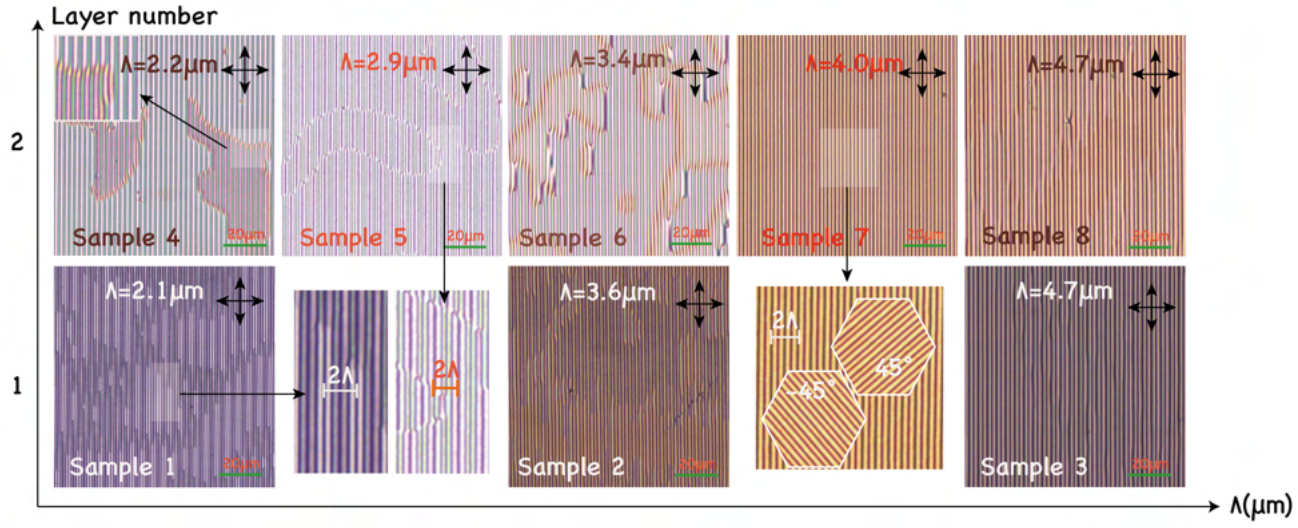

Fig. 3 Images of optical axis gratings from polarization microscope with crossed polarizers.

half wave plate, a beam expander and a polarizing beam splitter subsequently. It is split into two beams with perpendicular linear polarization direction. Both beams are converted to circularly polarized laser beams with opposite handedness by quarter wave plates and then interfere at the BY coated substrate surface. The half wave plate in the setup is used to tune the power of the two subsequent beams until they have exactly the same power. The sample is illuminated to achieve a UV dose of 17 J/cm^2. Figure 2 depicts two circularly polarized beams intersecting at a point. Where the two beams interfere, the resulting interference pattern consists of linear polarization that rotates continuously along the x direction. Over the distance of the UV laser wavelength λ_{UV} divided by $\sin(\theta_{UV}/2)$ the linear polarization direction rotates over a total angle of 360°. Since the BY is known to align the LC perpendicular to the linear polarization direction of the UV light, the LC will be aligned as shown in the illustration on the right. Note that the distance over which the LC rotates 360° is indicated as 2Λ. Optically there is no difference between LC orientations of 0° and 180°, which means that the optical period is Λ. The period of optical axis gratings can be changed by adjusting the angle between two UV laser beams according to the equation

$$\Lambda = \frac{\lambda}{2sin\frac{\theta_{UV}}{2}}. \quad (1)$$

2.2 Polymer layer

The mixture of reactive mesogens (RMs) contains 96% reactive mesogen RM257 (Haihang Industry), 2% photoinitiator Irgacure 819 (BASF) and 2% inhibitor tert-Butylhydroquinone (Sigma-Aldrich). The mixture is dissolved in toluene with a concentration of 20wt%. After the photoalignment step, the RM mixture is spincoated onto the BY layer with spincoating speed 3000 rpm for 30 s. Then, the samples are put into a chamber with quartz cover which is transparent to UV. The box is sucked vacuum, heated up to 80°C and illuminated with a mercury UV lamp. The illumination dose for polymerization step is maximum 8 J/cm^2. Careful analysis has revealed that the photopolymerization process does not alter the alignment imposed at the substrates by the previous UV illumination[12]. To make the polymer film thicker, another layer of the RM mixture can be spin coated and photopolymerized. In our experimental conditions, the thickness of one polymer layer is around 800nm and a double layer sample around 1600 nm. Under our experimental conditions, the previous layer of polymer is not affected by the subsequent spincoating process. The thickness was mechanically measured by a Veeco Dektak profilometer. Firstly we partially remove the polymer from the edge to create a height difference between polymer and glass substrate. Then we put the sample under the diamond needle of profilometer, align the sample edge with the needle and start to scan. By taking the height differences, the thickness of the polymer layer is obtained.

2.3 Samples

Table 1 Parameters of polymerized samples.

Sample	Period Λ (μm)	number of layers
1	2.1	1
2	3.6	1
3	4.7	1
4	2.2	2
5	2.9	2
6	3.4	2
7	4.0	2
8	4.7	2

In total 8 samples have been analyzed. The samples have a range of period Λ between 2 μm and 5 μm and consist of either 1 or 2 spin-coated layers of LC polymer. The details of these samples are shown in table 1.

3 Microscope analysis

Figure 3 shows the microscope pictures for each sample under crossed polarizers. As expected, all samples exhibit periodic patterns of bright and dark lines. Samples with large grating period

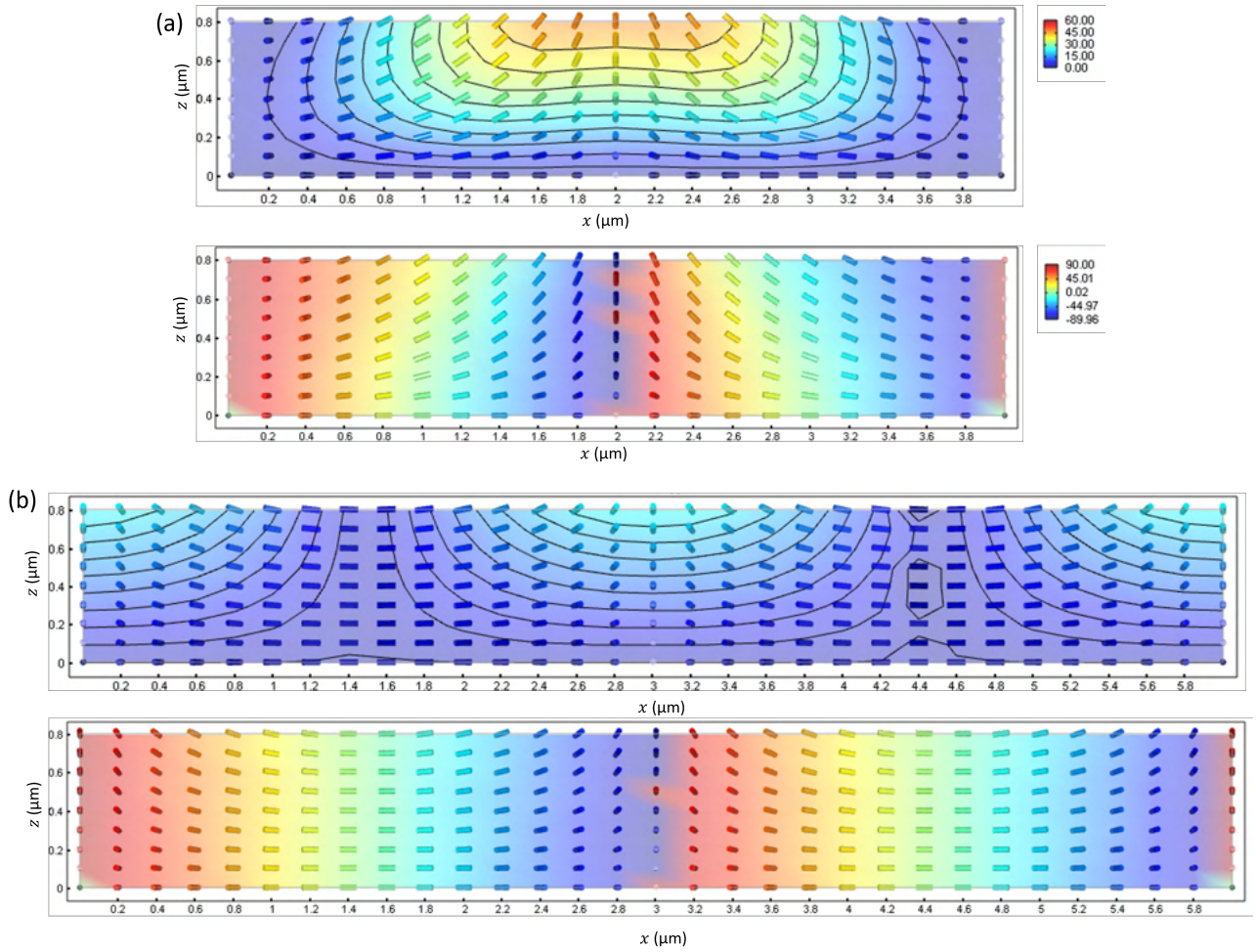

Fig. 4 Simulated director orientation for strong bottom anchoring and $W_{\text{top}} = 10 \times 10^{-6}$ J/m^2 for $2\Lambda = 4\mu$m (a) and $2\Lambda = 6$ μm (b). The top graph shows the tilt angle as colormap, the bottom figure the twist angle as colormap.

($\Lambda > 4$ μm, *i.e.* sample 3, 7 & 8) are fairly homogeneous and exhibit only one domain. Bright and dark lines alternatively occur and the width of these lines are equivalent. When these samples are rotated in a certain direction between the crossed polarizers, the bright and dark lines also rotate at the same velocity, the width of the lines remains the same and the lines move with a certain speed in one particular direction perpendicular to the lines. The overall average intensity of the sample remains the same. From the inset of sample 7 however, it is clear that not all bright lines have the same intensity. Typically one bright line with higher intensity is followed by a bright line with lower intensity in a periodic pattern.

The situation is different when observing the samples with Λ smaller than 4 μm. In these samples domains are visible. It appears that there are two distinct domains. The bright and dark lines are shifted when comparing the two domains. Sample 2 has bright and dark lines, but the bright lines have uneven brightness between domains. Some lines appear brighter than others. In addition to the brightness switching between domains, another unique feature occurs when Λ becomes less than 3 μm. Sample 5 has 2 layers of polymerized LC, which offers larger retardation. We can clearly see that the two adjacent bright lines have different color and the color switches if the line crosses the edge of the domain. The purple lines are thicker and the blue lines are thinner. Unlike the original one period length Λ with two bright lines, now the period becomes 2Λ with two blue lines plus two purple lines which means two adjacent Λ lengths are asymmetric. Two domains also appear in sample 1 and the asymmetry is observed again. The edges of domains are eased and quite wide where the period is Λ. The brightness of the bright lines is not uniform in the domains. If we look closely at the magnified part, in a period of 2Λ, one brighter line is followed by two less bright ones and finally by another bright one. Since the number of layers in sample 4 is doubled, the lensing effect of the rotating LCs becomes apparent. This makes it difficult to find a suitable focus to clearly show each 2Λ. When adjusting the focus of the microscope in sample 4, the edges of the domains are sharp and the color shift effect is very strong.

4 Q-tensor simulation

To investigate the distribution of the director orientation in the LC layer, simulations using a finite element Q-tensor method are performed[28–31]. As simulation space a length equal to 2Λ is taken, which is equivalent to a 360° rotation of the director at the sur-

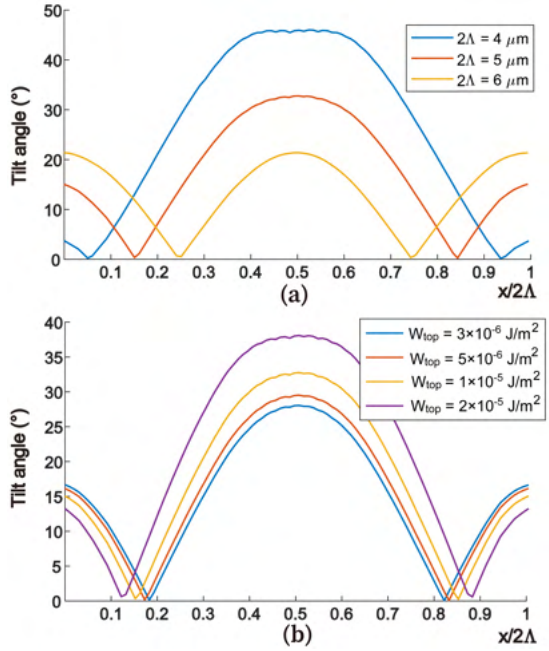

Fig. 5 (a) Simulated top surface tilt angle values from Q-tensor simulation for $2\Lambda = 4$ μm, 5 μm and 6 μm for strong bottom anchoring and weak homeotropic anchoring with $W_t = 1 \times 10^{-5}$ J/m^2. (b) Simulated top surface tilt angle for top surface anchoring energy $W = 3 \times 10^{-6}$ J/m^2, 5×10^{-6} J/m^2, 1×10^{-5} J/m^2 and 2×10^{-5} J/m^2 and $2\Lambda = 5$ μm.

face. Strong anchoring is imposed onto the substrate (the bottom surface) with zero pretilt angle, but also simulations with weak anchoring at the bottom surface will be discussed later. Weak homeotropic anchoring is imposed at the LC-air surface (top surface) with an anchoring strength that is in the order of what has been found for uniformly aligned polymer LC layers [12]. Because the material parameters of the RM257 material in the nematic LC phase have not been reported in literature, the elastic constants of E7 nematic LC have been used ($K_{11} = 11.1$ pN, $K_{22} = 6.5$ pN and $K_{33} = 17.1$ pN) [32]. For the optical simulations a birefringence of 0.18 is assumed.

The cross-section of a 0.8 μm thick LC layer is shown in Figures 4 for a period of $2\Lambda = 4$ μm (a) and $2\Lambda = 6$ μm (b). For each situation there are two pictures in which the director orientation at certain positions is visualized using cylinders. In the top picture, the colormap shows tilt angle, while in the bottom figure the colormap illustrates the twist angle. For both periods, we see an overall 360° azimuthal rotation of the director over the 2Λ distance. For $2\Lambda = 6$ μm this rotation is quite uniform along the thickness of the sample. For $2\Lambda = 4$ μm however, we see that variations in the twist angle occur when going from the bottom substrate towards the top. The tilt angle on the other hand shows even more interesting behaviour. First, it must be mentioned that due to the weak homeotropic anchoring strength at the LC-air interface, there is a nonzero tilt angle for both periods. Even with much lower homeotropic anchoring strength, the LC tends to tilt at the interface, as the structure contains a high amount of splay-bend energy. By tilting out of the xy-plane, twist elastic energy is introduced which in turn reduces the splay-bend elastic energy,

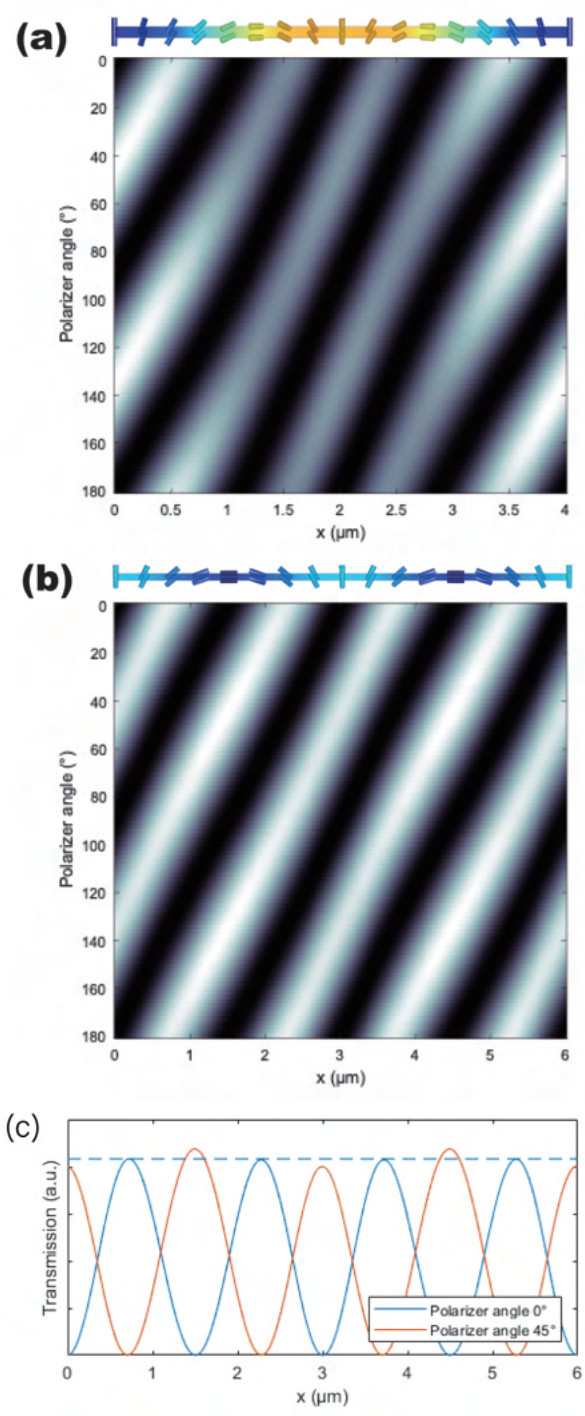

Fig. 6 Simulated optical transmission through crossed polarizers for $2\Lambda = 4$ μm (a) and $2\Lambda = 6$ μm (b) is shown for different angles of the polarizer. Both images have a top view schematic of the LC alignment orientation. (c) Simulated transmission curves for $2\Lambda = 6$ μm with polarizers at 0° and 45° respectively.

because $K_{22} < (K_{11}, K_{33})$ resulting in periodic asymmetry. This asymmetry is not present at the bottom (with fixed anchoring) and is getting stronger from the bottom to the surface. The presence of this asymmetric tilt angle further affects the twist angle.

Figure 5 shows the top surface tilt angle for different parameters. In Figure 5(a) the effect of the period is illustrated. For larger period ($2\Lambda = 6\ \mu$m) the top surface tilt angle is symmetric and the actual period of the structure is Λ. For smaller period ($2\Lambda = 4$ or $5\ \mu$m), the structure is asymmetric and the actual period of the structure is 2Λ. Nevertheless, for every period a non negligible tilt angle is obtained of more than 20°. Figure 5(b) demonstrates that the top surface tilt angle is affected by the value of the homeotropic anchoring strength at the top interface. But even with very small anchoring energy of 3×10^{-6} J/m^2 the top surface tilt angle reaches values of more than 25° for $2\Lambda = 5\ \mu$m).

An ideal optical axis grating with zero tilt and uniform rotation of the director has periodic bright and dark lines for crossed polarized transmission. When rotating the sample, the lines move along a certain direction and the intensity of the lines remain the same. The optical transmission in Figure 6 is obtained by a Jones calculus for three different wavelengths (blue, green & red) and combining this into a grey scale transmission image[33,34]. For a configuration with no asymmetry but nonzero top surface tilt, the 4 lines do not have exactly the same intensity, but the difference is not that big as can be observed in Figure 6(b) and (c). When rotating the sample (or equivalently, rotating both polarizer and analyzer over the same angle) the 4 lines move in a certain direction but again the intensity remains quite similar. For an asymmetric configuration, both the asymmetry of tilt angle and non uniform rotation of the twist angle results in two brighter lines and two darker lines in the interval $0 < x < 2\Lambda$. When rotating the sample, the bright lines turn into dark lines and vice versa, but the lines in the intervals $0 < x < \Lambda/2$ and $3\Lambda/2 < x < 2\Lambda$ are always brighter than the two lines in the interval $\Lambda/2 < x < 3\Lambda/2$.

Several parameters determine whether a configuration is symmetric or asymmetric. Since it is known that photoalignment has a finite anchoring strength also simulations are performed for weak anchoring at the bottom interface. Since the tilting of the director arises from an interplay between the homeotropic weak anchoring at the top, the planar anchoring at the bottom and the elastic deformation energy, it is clear that a weaker anchoring at the bottom interface will induce larger tilt angles at the top. As can be seen from Figure 7, a weak anchoring at the bottom interface also promotes the asymmetric configuration. The smaller the bottom anchoring strength, the more pronounced the asymmetric tilting becomes. More simulations about other parameters such as K22 (Figure S1 and S2) and smaller periods $2\Lambda = 3\ \mu$m and 2μm (Figure S3) refer to supplementary material.

5 Diffraction efficiency

To compare the diffraction efficiency between the samples with and without symmetry breaking, and subsequently to allow comparison of the impact of different thicknesses, we selected sample 1, sample 3 and sample 8 for further diffraction measurements. As shown in Figure 8, the efficiency of three representative LC

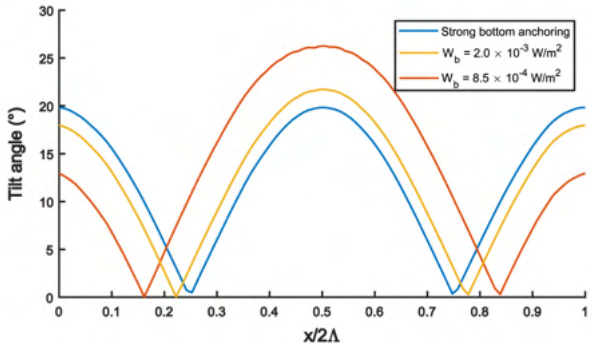

Fig. 7 Simulated top surface tilt angle values from Q tensor simulations for different anchoring conditions at the bottom surface. Top surface anchoring strength is 5×10^{-6} J/m^2 and $2\Lambda = 6\ \mu$m.

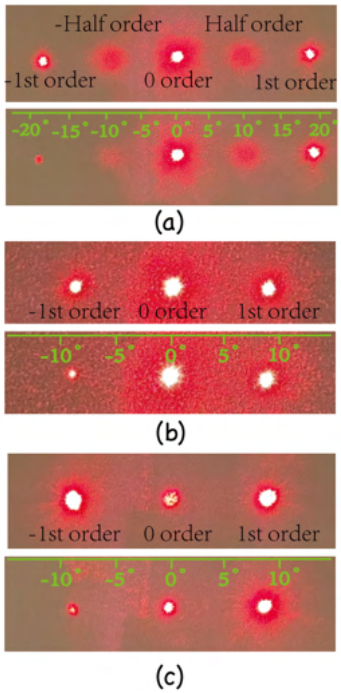

Fig. 8 Images of the laser spots on a white screen. Linearly (top figure) and circularly (bottom figure) polarized laser beams for sample 1 (a), sample 3 (b) and sample 8 (c).

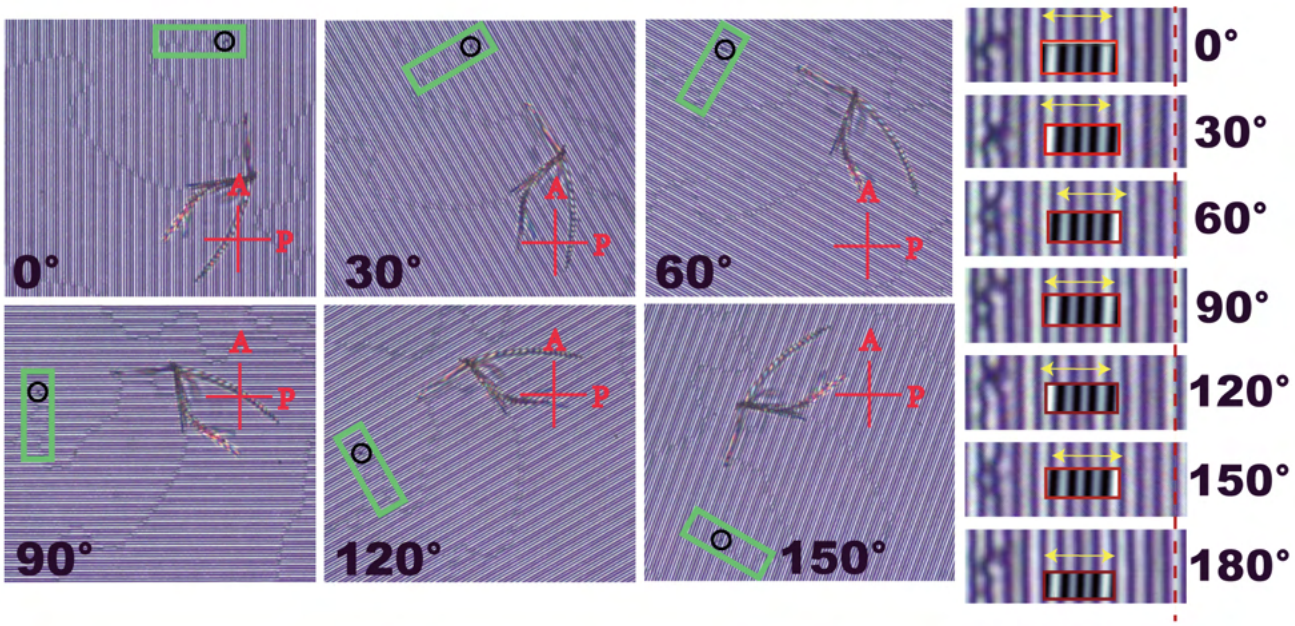

Fig. 9 Crossed polarizer images of sample 1 being rotated from 0° to 180° in 30° intervals. The right part shows a magnified view of the area indicated in green on the right. The red dashed line is vertical line that serves a guide for the eye. The red insets shows corresponding transmission data from simulation.

polarization gratings is measured for different diffraction orders of linearly and circularly polarized incident laser light (with 632 nm wavelength). The efficiency of a particular diffraction order is determined by dividing the measured power of that order by the total power of all transmitted diffraction orders. LC axis gratings have glass substrates without anti-reflection coatings, resulting in additional losses related to reflection. The results are listed in Table 2.

Table 2 Diffraction efficiencies of gratings.

Diffraction order		1	1/2	0	-1/2	-1
Sample 1	linear	17.2%	0.1%	65.6%	0.1%	17.2%
	circular	0.1%	0%	65.7%	0.1%	34.3%
Sample 3	linear	14.6%	0%	70.8%	0%	14.6%
	circular	0.8%	0%	70.8%	0%	28.3%
Sample 8	linear	46.7%	0%	7.2%	0%	46.7%
	circular	0.6%	0%	7.2%	0%	92.8%

6 Discussion

From the microscope images shown in Figure 3, the limit of the period at which LCs can be aligned to the desired alignment pattern is about 4 μm. The appearance of the domains is already occurring at a period about 3.5 μm, indicating the appearance of a tilt at the top surface. This coincides with the yellow line in Figure 5 (a). In samples with smaller periods, symmetry breaking can be observed and the doubling of the effective period to 2Λ, coinciding with the red and blue curves in Figure 5 (a).

When sample 1 is rotated between crossed polarizers from 0° to 180°, the same region in the sample can be cut and aligned based on the location of a particular defect and by examining the period of the sample. The full pictures are shown in Figure 9 on the left. The black circles indicate the position of the same defect on each picture. On the right hand side are the zoomed in and cut out regions from the green squares in the original pictures. They have been rotated back so the periodicity is again horizontal. The pictures in red squares are cut from the simulation data presented in figure 6(a). A red dashed line is placed in the middle of a bright lines for the angles 0°, 90° and 180° as a guide for the eye. Following the red dashed line, it is clear that the lines in the sample are continuously shifting to the left during rotation and the total shifted length is $\Lambda/2$ for 90° and Λ for 180°. The yellow double arrow lines indicate the unit cell length 2Λ. The position of simulated bright lines match very well with the experimental ones and the brightness variation follows a similar trend, which shows that the simulation model explains the phenomenon of symmetry breaking adequately. A video of the rotation is added in supporting information.

The symmetry breaking also affects the diffraction patterns as shown in Figure 8 for sample 1 (with symmetry breaking) and sample 3 & sample 8 (without symmetry breaking). If samples are illuminated by a linearly polarized laser beam, the beam is equally diffracted to the +1 and -1 order. Circularly polarized light is mostly diffracted to the +1 order. The first order efficiency of sample 8 is much larger than for sample 3 since the layer thickness is closer to the half-wave condition. There is still a considerable amount of power in the zero order for sample 8 since the thickness is still slightly too small. For 632 nm wavelength, the thickness should be around 1.76 μm (considering a birefringence of $n_e - n_o = 0.18$ for RM257). When the period of the grating becomes smaller, the diffraction angles become larger according to the well known diffraction equation $sin\theta_{out} = (m\frac{\lambda}{\Lambda}) + sin\theta_{in}$, where θ_{in} is the incident angle, θ_{out} is the diffraction angle of transmitted light, and m = -1, 0, +1 corresponding to the diffraction order.

However, because the apparent period has been doubled from Λ to 2Λ due to the symmetry breaking, also intermediate orders (½ and -½) occur between the 0 and the ± 1 orders shown in Figure 8 (a). From Table 2 we can see that the efficiency of half diffraction orders is relatively low compared to the first orders. The ± 1 order efficiency of sample 1 and sample 3 is lower than sample 8 because the thickness of the one-layer sample is much further away from the half wave thickness.

7 Conclusions

In this work, optical axis gratings with different periods are fabricated using a photopolymerized LC layer. Instead of performing the fabrication procedure in a glove box, the sample is prepared in ambient air and then photopolymerized in a vacuum chamber. Experimental analysis of all fabricated samples, together with director simulations, demonstrates that there is a considerable tilt angle of the LC near the LC-air interface. Moreover, for smaller periods, domains are observed in the samples that are attributed to a symmetry breaking effect in which regions with low and high pretilt are observed with an apparent period that is the double of the expected period. These experimental results can be explained by the director simulations by assuming that there is a small homeotropic weak anchoring energy at the LC-air interface.

Conflicts of interest

There are no conflicts to declare.

References

1 M. J. Escuti, J. Kim and M. W. Kudenov, *Optics and Photonics News*, 2016, **27**, 22–29.

2 M. Jiang, H. Yu, X. Feng, Y. Guo, I. Chaganava, T. Turiv, O. D. Lavrentovich and Q.-H. Wei, *Advanced Optical Materials*, 2018, **6**, 1800961.

3 H. Chen, Y. Weng, D. Xu, N. V. Tabiryan and S.-T. Wu, *Optics Express*, 2016, **24**, 7287–7298.

4 B. Gao, J. Beeckman and K. Neyts, *Crystals*, 2021, **11**, 220.

5 S. Slussarenko, A. Alberucci, C. P. Jisha, B. Piccirillo, E. Santamato, G. Assanto and L. Marrucci, *Nature Photonics*, 2016, **10**, 571–575.

6 Y.-H. Lee, G. Tan, T. Zhan, Y. Weng, G. Liu, F. Gou, F. Peng, N. V. Tabiryan, S. Gauza and S.-T. Wu, *Optical Data Processing and Storage*, 2017, **3**, 79–88.

7 S. Moon, C.-K. Lee, S.-W. Nam, C. Jang, G.-Y. Lee, W. Seo, G. Sung, H.-S. Lee and B. Lee, *Scientific Reports*, 2019, **9**, 6616.

8 B. Berteloot, I. Nys, X. Xue, J. Beeckman and K. Neyts, *Journal of Molecular Liquids*, 2021, **337**, 116238.

9 T. Zhan, J. Xiong, Y.-H. Lee and S.-T. Wu, *Optics Express*, 2018, **26**, 35026.

10 B. Berteloot, I. Nys, G. Poy, J. Beeckman and K. Neyts, *Soft Matter*, 2020, **16**, 4999–5008.

11 T. Zhan, J. Xiong, Y.-H. Lee, R. Chen and S.-T. Wu, *Optics Express*, 2019, **27**, 2632–2642.

12 X. Xue, B. Berteloot, M. Stebryte, K. Neyts and J. Beeckman, *Optical Materials Express*, 2021, **11**, 4036–4050.

13 M. Mohammadimasoudi, K. Neyts and J. Beeckman, *Proc. SPIE*, 2015, 93840E.

14 M. López-Valdeolivas, D. Liu, D. J. Broer and C. Sánchez-Somolinos, *Macromolecular Rapid Communications*, 2018, **39**, 1700710.

15 C. Provenzano, P. Pagliusi and G. Cipparrone, *Optics express*, 2007, **15**, 5872–8.

16 M. Wang, Y. Li and H. Yokoyama, *Nature Communications*, 2017, **8**, 388.

17 G. P. Crawford, J. N. Eakin, M. D. Radcliffe, A. Callan-Jones and R. A. Pelcovits, *Journal of Applied Physics*, 2005, **98**, 123102.

18 V. Nersesyan, I. Nys, F. Van Acker, C.-T. Wang, J. Beeckman and K. Neyts, *Journal of Molecular Liquids*, 2020, **306**, 112864.

19 I. Nys, J. Beeckman and K. Neyts, *Soft Matter*, 2015, **11**, 7802–7808.

20 I. Nys, V. Nersesyan, J. Beeckman and K. Neyts, *Soft Matter*, 2018, **14**, 6892–6902.

21 M. Nieborek, K. Rutkowska, T. R. Woliński, B. Bartosewicz, B. Jankiewicz, D. Szmigiel and A. Kozanecka-Szmigiel, *Crystals*, 2020, **10**, 768.

22 M. J. Escuti, C. Oh, C. Sánchez, C. Bastiaansen and D. J. Broer, Imaging Spectrometry XI, 2006, pp. 21–31.

23 K. Gao, H.-H. Cheng, A. K. Bhowmik and P. J. Bos, *Optics Express*, 2015, **23**, 26086.

24 X. Xiang, J. Kim, R. Komanduri and M. J. Escuti, *Optics Express*, 2017, **25**, 19298–19308.

25 M. Stebryte, I. Nys, Y. Y. Ussembayev, J. Beeckman and K. Neyts, *Crystals*, 2020, **10**, 807.

26 Y.-H. Lee, Z. He and S.-T. Wu, *JOSA B*, 2019, **36**, D9–D12.

27 Y. Weng, Y. Zhang, J. Cui, A. Liu, Z. Shen, X. Li and B. Wang, *Optics Letters*, 2018, **43**, 5773–5776.

28 R. James, E. Willman, F. FernandezFernandez and S. Day, *Electron Devices, IEEE Transactions on*, 2006, **53**, 1575–1582.

29 M. Ravnik and S. Žumer, *Liquid Crystals*, 2009, **36**, 1201–1214.

30 D. M. Sussman and D. A. Beller, *Frontiers in Physics*, 2019, **7**, 204.

31 S. Bartels and A. Raisch, *Singular phenomena and scaling in mathematical models*, Springer, 2014, pp. 383–412.

32 S. W. Leonard, J. P. Mondia, H. M. van Driel, O. Toader, S. John, K. Busch, A. Birner, U. Gösele and V. Lehmann, *Physical Review B*, 2000, **61**, R2389–R2392.

33 G. Panasyuk, J. Kelly, E. C. Gartland and D. W. Allender, *Physical Review E*, 2003, **67**, 041702.

34 P. W. Ellis, E. Pairam and A. Fernández-Nieves, *Journal of Physics D: Applied Physics*, 2019, **52**, 213001.